Kai et al. *Quantum Frontiers* (2025) 4:2
https://doi.org/10.1007/s44214-025-00075-7

Quantum Frontiers

ORIGINAL ARTICLE Open Access

Distinct moiré exciton dynamics in WS_2/WSe_2 heterostructure

Feng Kai[1], Xiong Wang[1], Yiqin Xie[1], Yuhui Yang[1], Kenji Watanabe[4], Takashi Taniguchi[4], Hongyi Yu[2,3], Wang Yao[1] and Xiaodong Cui[1*]

Abstract

This letter reports a time resolved pump-probe reflectance spectroscopic study on moiré excitons in a twisted monolayer WS_2/WSe_2 heterostructure. By probing at the resonant energies of intralayer excitons, we observed their distinct temporal tracks under the influence of interlayer excitons, which we attribute to the discrepancy in spatial distribution of the intralayer excitons in different layers. We also observed that intralayer moiré excitons in WSe_2 layer differ at decay rate, which reflects different locations of Wannier-like and charge-transfer intralayer excitons in a moiré cell. We concluded that the interlayer moiré excitons form within a few picoseconds and have the lifetime exceeding five nanoseconds. Our results provide insights into the nature of moiré excitons and the strain's significant impact on their behaviour in twisted heterostructures, which could have important implications for the development of novel optoelectronic devices.

Keywords: Exciton dynamics, Moiré exciton, 2D semiconductor, van der Waals heterostructure

1 Introduction

The emergent van der Waal (vdW) heterostructures provide a platform that allows manipulation of various degrees of freedoms and creation of artificial lattices. The deliberate lattice mismatch between individual vdW layers engenders a periodic interference pattern, known as the moiré pattern. This tailored moiré pattern offers a great flexibility of building artificial superlattices and has invoked fantastic quantum states including superconducting, fractional quantum anomalous Hall, strongly correlated states, etc [1–11]. One of the intriguing topics is the exciton physics in moiré superlattices, particular TMD moiré superlattices which feature direct bandgap in monolayers and rich degrees of freedoms. Predominantly, TMD heterostructures display a type-II quantum well band alignment, with conduction and valence band edges residing in disparate layers. Consequently, photocarriers, upon optical excitation, swiftly relax to the disparate band edges through interlayer charge transfer, culminating in the formation of interlayer excitons (IX). The spatial separation in these structures renders the interlayer excitons an extended lifetime, often reaching several nanoseconds [12, 13] and ultralong valley lifetime around 40 μs [14, 15]. This long-life significantly lowers the barriers towards quantum phase transitions. In moiré superlattices these interlayer excitons modulated by the periodic moiré potentials display exotic features originating from the unique dispersion in the superlattice. Besides the moiré potential from the heterostructure stacking, the in-plane strain in individual layer arising from the lattice mismatch also contributes to the moiré potential modulation [16–24]. Given the disparity in Young's modulus and fracture strength [25], the strain within each heterostructure layer varies in intensity. For interlayer excitons, this results in electrons and holes in opposing layers experiencing distinct in-plane moiré potential modulations. These multifaceted moiré potentials complicate the microscopic understanding of moiré excitons. The pump-probe study has flexibility to tune the probed energy, enabling the study

*Correspondence: xdcui@hku.hk
[1] Physics Department and HK Institute of Quantum Science & Technology, The University of Hong Kong, Pokfulam road, Hong Kong, China
Full list of author information is available at the end of the article

of interactions between IX and various excitons in the moiré superlattices, providing insightful microscopic understanding. As yet, the pump-probe study of moiré excitons remain largely unexplored.

The lack of pump-probe study of the interlayer moiré excitons partially results from the relatively weak oscillator strength of the interlayer excitons. The spatial separation reduces the electron-hole wave function overlap and weakens the oscillator strength of interlayer excitons. Consequently, interlayer exciton is usually invisible in the reflection/absorption spectra which violates the prerequisite of pump-probe measurement. In this letter, we report a time-resolved pump-probe reflection spectroscopic study on moiré excitons of the twisted monolayer WSe_2/WS_2 heterostructure. We probed the reflectance spectra at the resonant energies of WSe_2 and WS_2 intralayer excitons and observed the different carrier dynamic patterns. These different dynamics reflect the coupling between intralayer excitons and interlayer excitons in a moiré cell, respectively. Our findings reveal a significant in-plane moiré strain in WSe_2 layer and the difference in WSe_2 and WS_2 intralayer excitons under the strain modulation.

2 Fabrication

Monolayer WSe_2 and WS_2 were mechanically exfoliated from single crystal and were vertically stacked as a heterostructure with a twist angle of around 0.8°. The heterostructure was encapsulated single crystal hexagonal boron nitride (h-BN) nanoflakes, then the whole stack was transferred onto a silicon substrate with 90 nm silicon dioxide cap-layer (Fig. 1a). The twist angle between the monolayer WS_2 and WSe_2 was identified by the polarization-dependent second harmonic generation (SHG) measurement (Data shown in Fig. 1). The two slightly mis-aligned six-fold SHG patterns were clearly observed (three folds is shown here), and the six-fold fitting revealed the relative twist angle of 0.8°. The heterostructure yields a stronger SHG intensity (Fig. 1b) than both individual monolayer WSe_2 and WS_2, indicating the heterostructure has AA stacking configuration (R-stacking).

3 Interlayer exciton

Figure 1c shows the photoluminescence spectra collected on the heterostructure and monolayer WSe_2 at the base temperature of 20K. The photoluminescence peaks (red) of neutral excitons at 1.734 eV and trions (charged exciton) at 1.698 eV of monolayer WSe_2 fade in the heterostructure as a consequence of interlayer charge transfer. This is consistent with the type-II band alignment (Fig. 1d) in which the minimum of conduction band is located at K (K') valley of WS_2 and the maximum of valence band at WSe_2 layer. Under optical excitation, most intralayer electron-hole pairs are disassociated and drift to opposite layers, namely, holes transferring to WSe_2 while electrons to WS_2. This interlayer charge transfer takes place in around hundreds of femtoseconds [26–30] which is a few orders of magnitude faster than the intralayer exciton lifetime, consequently, quenches the PL of intralayer excitons. The band edge electron-hole pairs at different layers are bonded to form interlayer excitons, identified as the peaks around 1.395 eV (Fig. 1c, black).

4 Ladder-like interlayer exciton emission

To further investigate the interlayer exciton in our device, we did a series of intensity-dependent photoluminescence measurements. Figure 2a presents photoluminescence of interlayer excitons at different excitation intensities. Due to the interference of our CCD device at the specific wavelength, the raw data (grey lines) carries significant interference patterns. To remove artificial device noise, we use multi-peak Lorentz fitting to extract the PL spectra. We observed that there's only one interlayer exciton emission peak (IX_1) at 1.388 eV under low excitation intensity of 0.1 $\mu W/\mu m^2$ (Fig. 2a, black line). As the excitation intensity increases to 17 $\mu W/\mu m^2$, the second interlayer emission peak (IX_2) arises at the energy 37 meV higher than IX_1 (blue line). Under low excitation intensity, the interlayer excitons density, or the filling factor (the number of excitons per moiré unit cell), is low, and the exciton-exciton interaction is negligible. As the excitation intensity increases, the interlayer excitons populates and the exciton-exciton interaction arises. When the filling factor is above 1, namely, every moiré cell has one exciton and some moiré cells has to accommodate two excitons, the exciton energy is lifted owing to the onsite dipole-dipole repulsion. This is well described by the exciton Hubbard model [31]. Our photoluminescence experiment indicates an onsite dipole-dipole repulsion energy (U) of 37 meV, which manifests as the energy jump from IX_1 to IX_2 (Fig. 2b), qualitatively consistent with the previous reports [31]. With such understanding, the thirdly and fourthly occupied moiré cell correspond to IX_3 and IX_4, with the energy jump of ΔE_{32} = 29 meV and ΔE_{43} = 49 meV, shown in Fig. 2b. Besides the energy jump between *IXs*, all the four peaks blue-shift with the increasing excitation intensity from 0.1 to 362 μW. The blue shift originates from long-range dipolar repulsion between interlayer excitons trapped in the neighboring moiré cell [31].

5 Reflection contrast

We then characterized the absorption by static reflection contrast spectroscopy. Figure 2c shows the background-free reflection contrast (RC) of the heterostructure device and monolayers. Here, the RC is obtained by $R/R_0 - R_{bg}$, where R and R_0 are the reflection spectrum of the heterostructure device and its hBN-only region, and R_{bg} is the background in RC due to substrate interference. We found the A exciton absorption peak (1.727 eV, red line) of monolayer WSe_2 splits into three peaks (with the energies of 1.683 eV, 1.742 eV and 1.784 eV, labelled as I, II,

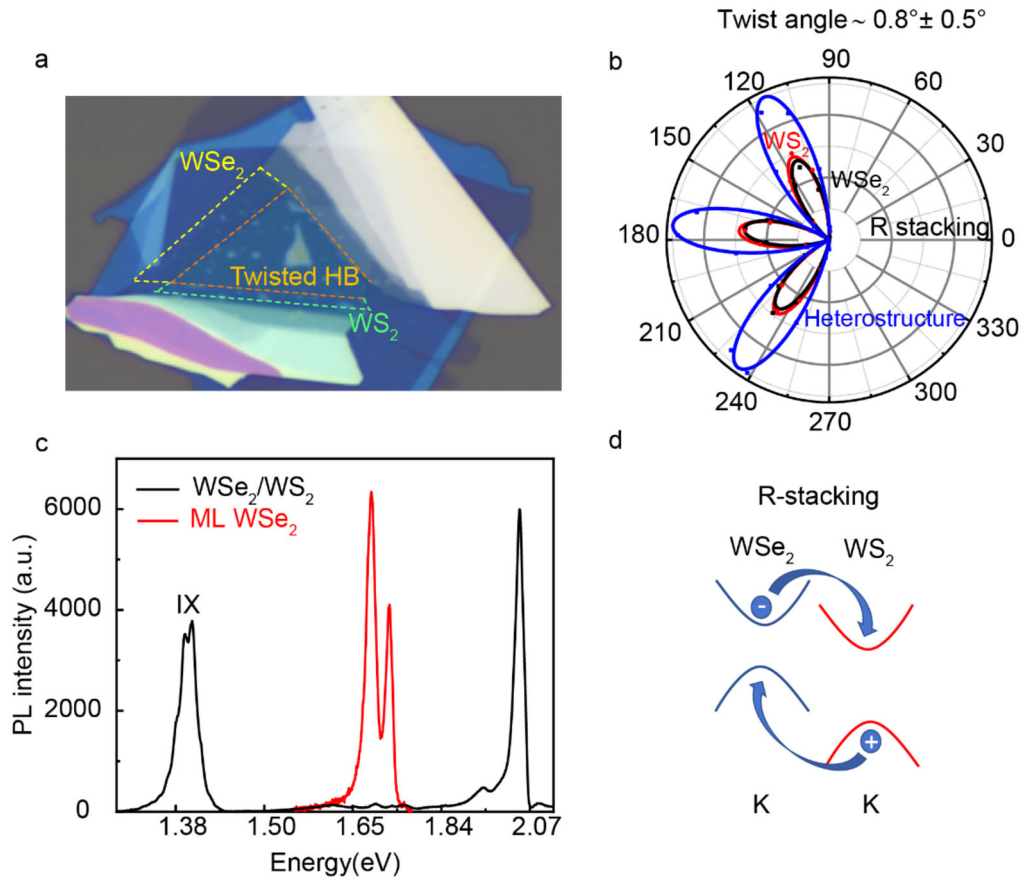

Figure 1 a, Optical microscopic image of the device. Heterostructure, monolayer WSe_2 and WS_2 region are outlined by orange, yellow and black dash line, respectively. b, Polarization-resolved SHG of individual monolayers WSe_2 (yellow), WS_2 (green) and heterostructure (orange). The relative twist angle is extracted to be 0.8° ± 0.5° by fitting. c, Photoluminescence of monolayer WSe_2 (red) and WSe_2/WS_2 heterostructure device (black) under 2.087 eV (594 nm) excitation at intensity of 5 μW. The interlayer exciton peak appears at 1.395 eV, labelled as *IX*. d, Diagram of the electron and hole transfer in type-II band alignment

III, respectively) in the heterostructure. These emergent three peaks were previously observed and attributed to the unique moiré exciton feature in WSe_2/WS_2 heterostructure [32]. It was interpreted with the continuum model that the emergent periodic moiré potential modifies the excitonic dispersion, splitting the edge into three sub bands, contributing to the observed three peaks [32–34].

However, we also note that the WS_2 layer, sharing the moiré pattern with WSe_2, does not experience splitting. This could be attributed to the different in-plane strain patterns in the two layers under the lattice reconstruction [23]. It has been shown that, in a rigid moiré landscape without the lattice reconstruction, the moiré potential experienced by intralayer excitons in either layer is very weak [35]. When structure relaxation is taken into account, the resultant periodic strains can give rise to pronounced modulation of electronic band structures and the energy landscape of the intralayer exciton [36]. Driven by the stacking-dependent interlayer van der Waals interaction, the WS_2/WSe_2 heterostructure, once fabricated, would experiences a structural reconstruction [23]. Given the WS_2 has higher Young's modulus (302 GPa) and fracture strength (47 GPa) than WSe_2 (258 GPa and 38 GPa) [25], WSe_2 and WS_2 experience different extent of lattice reconstruction and the in-plane strain modification. The discrepancy in intralayer exciton splitting demonstrates that a stronger strain pattern is generated in the WSe_2 layer upon the lattice reconstruction, giving rise to the strong moiré potential and miniband splitting for WSe_2 exciton, while the strain in WS_2 layer is not strong enough to split its intralayer exciton dispersion. We further infer that the WS_2 intralayer exciton remains largely similar to that in pristine WS_2 monolayer due to its strong mechanical strength.

6 Pump probe spectroscopy on moiré superlattice

After characterising the effects of moiré landscape on the intralayer excitons in our device from the photolu-

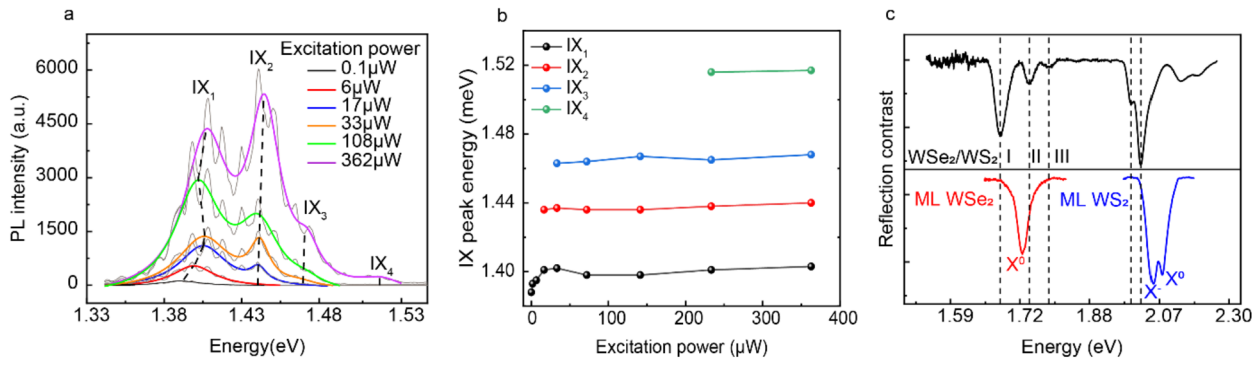

Figure 2 Photoluminescence and reflection contrast spectra of WSe_2/WS_2 moiré superlattice at 20K. a, Excitation intensity-dependent interlayer exciton photoluminescence: raw data (grey lines) and the corresponding Lorentz fitting curves (colour lines). The obtained four interlayer exciton peaks, labelled as IX_1 to IX_4, are outlined by dashed black lines, respectively. b, Extracted IX peak energies vs excitation intensity from Fig. 2a. c, Background-free reflection contrast (RC) of the WSe_2/WS_2 device (top, black). In the bottom, RC of monolayer WSe_2 (red) and WS_2 (blue). The intrinsic WSe_2 *A* exciton at 1.727 eV (718 nm) splits into three n resonances in the heterostructure, labelled as I, II, III. Three resonances have energies of 1.784 eV (695 nm), 1.742 eV (712 nm), 1.683 eV (737 nm), respectively

minescence and reflection contrast spectra, we investigate the moiré exciton dynamics by pump probe spectroscopy. Since the interlayer exciton has very weak oscillator strength, the pump probe spectroscopy that based on reflection change can't capture it directly. Instead, we probe around the resonant energies of the intralayer excitons of WSe_2 and WS_2. Here we pump the heterostructure with a beam of 3.1 eV (400 nm) at 100 $\mu W/\mu m^2$ that is energetic enough to excite all low-energy transitions. The hot photo-carriers, electron-hole pairs, thermally relax in the first hundreds of femtosecond [37, 38], followed by charge transfer and interlayer exciton formation in around 1 ps [39]. Owing to the type-*II* band alignment in WSe_2/WS_2, the IX's electrons (holes) reside in the conduction band of WS_2 layer (valence band of WSe_2 layer), which share the same band as the intralayer excitons of individual layers. By probing at the intralayer excitons, we can monitor the dynamics of the electron or hole components of moiré interlayer excitons, namely, we monitor the impact of pump-induced interlayer excitons on the intralayer exciton transitions.

7 Probe around resonance of WS_2 intralayer excitons

Figure 3a shows the pump-induced reflection change (dR/R) as a function of the delay time and the probe energy across the range of the WS_2's intralayer exciton transition. The transient reflectance of $dR/R > 0$ represented by bright-colored region implies that the sample reflectance increases under the increased pump excitation intensity, and vice versa. To analyze the dR/R map, we horizontally slice the dR/R map at different delay time (Fig. 3b) to get the profile of dR/R versus energy. We notice that the dR/R prior to the pump-probe coincidence $t = 0$ shows a non-zero value, significantly higher than the background noise. As the laser pulse repeats with a time interval of 13.2 ns (76 MHz), the non-zero dR/R at $t < 0$ indicates that a significant portion of interlayer excitons survive longer than 13.2 ns. Since the profile of dR/R *vs* energy is influenced by the resonant energy shift and the suppression of neutral exciton (X^0) and trion (X^-) oscillator strength owing to state filling. To quantitatively extract the energy shift, we append the pump induced reflection change (dR) to the static reflection contrast (R/R_0), constructing the dynamic reflection contrast at various time (Fig. 3c). With Lorentz fitting, we extract the evolution of the energy shifts for the absorption peaks (Fig. 3d). The energy shifts of both resonances show flat decay pattern in the probe time ranging from $t = 20$ ps to 80 ps (Fig. 3d), which is another evidence for interlayer excitons' long lifetime. In contrast, the exciton lifetime in monolayer WS_2 determined by the pump-probe spectroscopy is around 10^2 ps [40]. This long lifetime probed at the resonant energy of *A* exciton doesn't reflect the dynamics of intralayer excitons in WS_2 layer. Instead, this probe at intralayer exciton energy reflects the lifetime of the interlayer excitons as the interlayer excitons and delocalized intralayer excitons of WS_2 layer share the same electron orbits. This provides an easy approach to address the dynamics of interlayer exciton with pump-probe spectroscopy.

8 Probe around the resonance energy of WSe_2 intralayer excitons

We probed the WSe_2's intralayer exciton transition to investigate the influence of moiré interlayer excitons on WSe_2. We observed a negative dR/R region from 1.65 to 1.68 eV (Fig. 4a, dark region) accompanied by a strong positive region from 1.68 to 1.72 eV (Fig. 4a, bright region), a trend that is clearly visible in the cross-cutting diagram

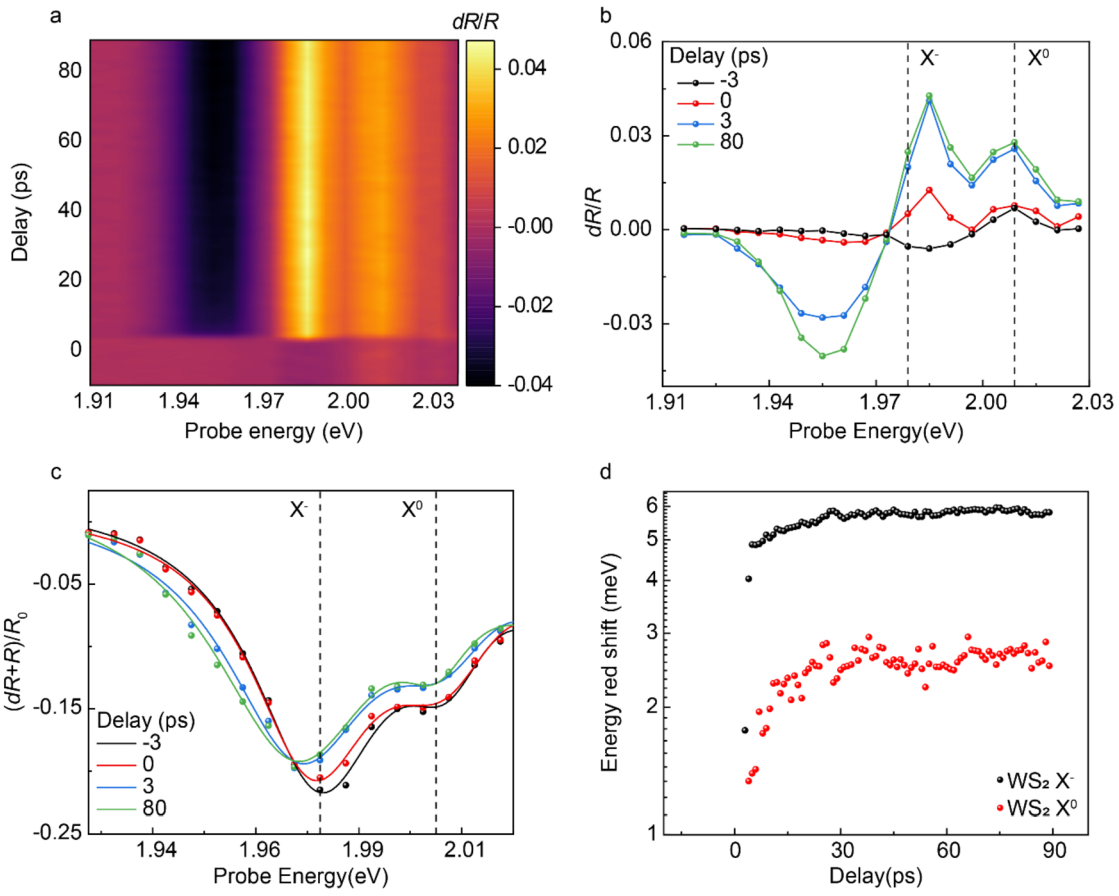

Figure 3 Pump probe spectroscopy for WS_2 intralayer transitions. a, Pump-induced reflection change map (dR/R) as a function of delay and probe energy, where R is the reflection spectra of twisted WSe_2/WS_2 heterostructure. b, dR/R vs Probe energy at −3, 0, 3, 80 ps. The neutral exciton (X^0) and Trion (X^-) is labelled with dash line for reference. c, Reflection contrast at different delays. d, Energy red shift vs delays for the neutral exciton (X^0) and Trion (X^-)

(Fig. 4b). This can be explained by the red shift and suppression of moiré resonance I, as diagramed in Fig. 4c. Another positive region appears in the range from 1.73 to 1.8 eV, covering both resonance II and III. To quantitatively extract the energy shift and absorption suppression, we use the same method as we did in WS_2 to get the reflection contrast at various delays, $(dR + R)/R_0$, as presented in Fig. 4d, and then extract the energy shifts and the amplitude suppression with Lorentz line shape fitting.

We found that peak I and II red shift, and in contrast, the peak III blue shifts upon pump (Fig. 4e). Here we consider several possible mechanisms for the energy shift: (1) The bandgap renormalization [41, 42] caused by Coulomb screening of free carriers or excitons on Coulomb repulsion in lattice, resulting in electronic bandgap shrink. (2) The screening effect [43–45] caused by exciton or free carrier's Coulomb screening on exciton which reduces the exciton binding energy and makes the exciton resonant energy blue shift. Since the moiré exciton III has larger Bohr radius (around 5 nm) than moiré exciton I (tightly bound) [36], exciton III is more sensitive to the dielectric environment and consequently experiences stronger charge-exciton and exciton-exciton screening effect. The significantly higher Coulomb screening on large Bohr radius excitons might be the reason for the blue shift. The sensitivity of large Bohr radius exciton to Coulomb screening is well known and one has utilized the energy shift of 2 s exciton with large Bohr radius (∼6 nm) as a sensor to monitor metal-insulator Mott transition in WSe_2/WS_2 moiré superlattice [7]. (3) The exciton-exciton interaction [12, 35], which includes a dipole-dipole interaction term and an exchange interaction term. The dipole-dipole interaction between intralayer and interlayer excitons is close to zero, as the intralayer exciton has no static electric dipole. Meanwhile, the exciton-exciton exchange interaction relies on wavefunction spatial overlap [31, 46]. Particularly, the intralayer moiré excitons could have sizable spatial overlap with the interlayer moiré excitons when their hole con-

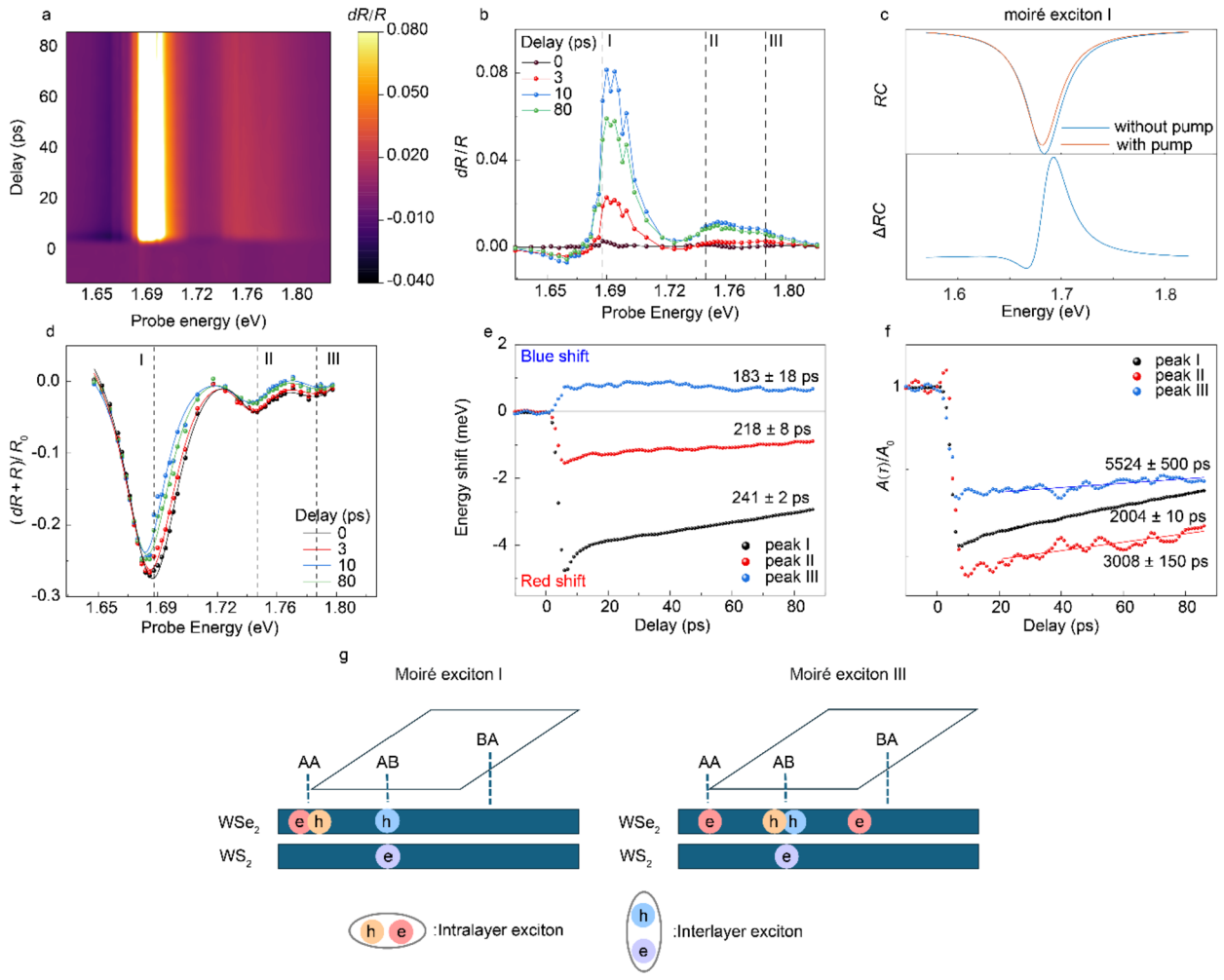

Figure 4 Pump probe spectroscopy for WSe_2 intralayer transitions. a, Pump-induced reflection change map (dR/R) as a function of delay time and the probe energy. b, dR/R vs Probe energy at 0, 3, 10, 80 ps. The moiré excitons I, II and III are labelled with dash line for reference. c, Schematic of the dR/R curve as a result of energy shift and suppression of absorption peak. d, Dynamics of the reflection contrast, $(dR + R)/R_0$, at various delay times. The Lorentz line shape fitting (colour lines) gives the evolution of three moiré excitons. e, Extracted energy red shift as a function of delay time for three moiré excitons. f, Extracted absorption amplitude, $A(\tau)/A_0$, as a function of delay time for three moiré excitons. $A(\tau)$ is the absorption amplitude at delay τ, A_0 is a constant represents the amplitude before the pump excitation. The vertical axis is in log scale and red straight lines presents single exponential fitting. The lifetimes probed at the resonance energies of three excitons are estimated through single exponential fitting. g, Schematic of the Spatial distribution for interlayer exciton and intralayer moiré excitons [36, 47]

stituents are both in WSe_2. The lowest-energy interlayer excitons generated by the pump beam would have their maximum intensity reside around R_h^X site (Fig. 4g); For intralayer moiré exciton I, its electron and hole both reside around R_h^h site that has small spatial overlap with interlayer excitons (Fig. 4g, moiré exciton I), so exchange interaction is negligible here. By contrast, moiré exciton III has its hole in R_h^X site, occupying the same site with the hole of interlayer exciton (Fig. 4g, moiré exciton I), where the exchange interaction can arise from the exchange of holes [35]. The exchange interaction between lowest-energy interlayer exciton and intralayer moiré exciton III tends to increase their total energy [31, 46], which is one possible reason for the blue shift of moiré exciton III. Our observations suggest that the bandgap renormalization effect dominates for moiré exciton I and II, while exciton-exciton screening and exchange interaction effects may dominate for exciton III.

Moiré exciton I, II and III's absorption are all suppressed due to state filling of the interlayer excitons, and their decay rate are approximately within the same orders of magnitude, with minor variations (Fig. 4f). The moiré exciton I (black) shows a faster decay rate than the moiré exciton III (blue). To understand the difference in decay rate, we fol-

low the spatial overlap picture of intralayer and interlayer excitons [36, 47]. In our understanding, the spatial overlap between the holes of intralayer and interlayer excitons determines the extent of absorption suppression. The more spatial overlap between the two holes of intralayer and interlayer excitons, the more suppression for the intralayer transition. After the pump excitation, the hot interlayer excitons would thermalize and follow a thermal distribution near the band edge within sub-picosecond [48]. In real space picture, the lowest-energy interlayer exciton has its hole localized in the R_h^X site [47], which barely overlaps with intralayer moiré exciton I that has hole in the R_h^h site, but overlap significantly with moiré exciton III that has its hole also in R_h^X site. As for the hot interlayer exciton that has extra kinetic energy, it tends to be more delocalized, contributing to overlap with the hole of exciton I in R_h^h site. As the assembly of interlayer excitons further cool down, their spatial distribution gradually shrinks to the R_h^X site, leading to a gradual decrease of the spatial overlap between the holes, accompanied by the recovery of moiré resonance I, which would account for the difference in decay rate.

9 Discussion

We observed a noticeable discrepancy between the dynamics probed at the resonant energies of WS_2 and WSe_2 intralayer excitons. The lifetime probed at resonant intralayer excitons of WS_2 is longer than that of WSe_2. As the photo carriers exist in the form of interlayer excitons, the probe at the intralayer exciton energy measures the wavefunction overlap between intralayer excitons (probe) and occupied interlayer excitons. Specifically, the data reflects the wavefunction overlap between the electron (hole) component of intralayer excitons in the WS_2 (WSe_2) layer and its counterpart in the interlayer excitons. Note that the interlayer exciton has its electron and hole localized around the R_h^X site [47]. The photoluminescence and reflection contrast measurements (Fig. 2) indicate that due to the in-plane periodic strain introduced by the lattice reconstruction, the intralayer exciton in WSe_2 layer splits into three moiré excitons (I, II and III). On the other hand, the intralayer exciton in WS_2 layer is not much different from that in a pristine layer, spreading uniformly across the moiré cell. The reflection probed at intralayer exciton resonance in WS_2 layer well captures the interlayer exciton lifetime. By contrast, the intralayer moiré excitons in WSe_2 layer are localized with distinct spatial profiles within a moiré cell [36]. Especially, exciton I resides at R_h^X site, away from the lowest-energy interlayer exciton in spatial distribution. For excited interlayer excitons carry extra energies [46], they can have extended distributions and therefore build a sizable spatial overlap with the hole component of the intralayer exciton I. As interlayer excitons further cool down and their wave function intensities concentrate around the R_h^X site, the overlap with intralayer excitons I gradually shrinks and it displays a fast decay rate. Therefore, the signal probed at intralayer exciton I energy primarily reflects the cooling process of interlayer excitons. Intralayer exciton III, however, tends to reside at R_h^X site and shares the similar hole component spatial distribution as the lowest-energy interlayer exciton. Therefore, the probe at intralayer exciton III shows a slower decay rate than that at intralayer exciton I. Nonetheless, its decay pattern is still different from that probed at WS_2 intralayer exciton. This could be attributed to the weak signal *vs*. noise ratio data at WSe_2 intralayer exciton III owing to it weak oscillator strength. Or the hole components at interlayer exciton and WSe_2 intralayer exciton III are located at different sub-bands. This needs further investigation.

Yet we cannot quantitatively extract the interlayer exciton lifetime in probing at WS_2 intralayer exciton energy, for the nearly zero decay pattern in the detection time range. The lower bound that we can determine is approximately from the exciton III's decay pattern. Given exciton III occupies the same site with lowest-energy interlayer excitons, exciton III's lifetime reflects interlayer exciton lifetime. Therefore, we infer that the interlayer exciton lifetime exceeding 5 ns.

10 Conclusion

In this work, we observed that a near-zero twisted WSe_2/WS_2 heterostructure exhibits spectroscopic features modulated by a signature moiré potential: the ladder-like interlayer photoluminescence and the splitting of moiré intralayer excitons in WSe_2 layer. The former reveals the on-site exciton-exciton repulsion between moiré interlayer excitons localized at the same site, while the latter reflects the influence of moiré potential and in-plane strain modification on exciton dispersion. The distinct splitting behaviours in absorption spectra and the slow decay pattern in the pump-probe spectra indicate that the intralayer exciton is delocalized in WS_2 layer and the intralayer moiré excitons in WSe_2 layer tend to be localized at different sites in the moiré cell, as a result of different in-plane strain and reconstruction. Our pump-probe data confirms that the moiré interlayer exciton experiences a few picoseconds cooling-down time and a lifetime exceeding five nanoseconds. Our study provides a comprehensive approach to investigate the dynamics of moiré interlayer excitons.

Acknowledgements

The work was supported by the National Key R&D Program of China (2020YFA0309600), Guangdong-Hong Kong Joint Laboratory of Quantum Matter, the University Grants Committees/Research Grants Council of Hong Kong SAR (AoE/P-701/20, 17300520, 17301223) and the Theme Research T45-406/23-R, MOST 2023ZD0300600. K.W. and T.T. acknowledge support from the Elemental Strategy Initiative conducted by the MEXT, Japan (Grant Number JPMXP0112101001) and JSPS KAKENHI (Grant Numbers 19H05790, 20H00354 and 21H05233). H.Y. acknowledges support by NSFC under Grant No.

12274477 and the Department of Science and Technology of Guangdong Province in China (No. 2019QN01X061).

Author contributions
X.D.C and K.F conceived the research. K.F, X.W, Y.Q.X and Y.H.Y fabricated van der Waals heterostructures. K.W. and T.T. grew hexagonal boron nitride crystals. K.F carried out optical measurements. X.D.C, K.F., X.W performed data analysis and interpreted the results. X.D.C, K.F., W.Y and H.Y.Y wrote the paper with input from all authors. All authors discussed the results.

Data availability
The authors confirm that the data supporting this study are available within the manuscript. Raw data are available upon the request.

Declarations

Competing interests
The authors declare no competing interests.

Author details
[1]Physics Department and HK Institute of Quantum Science & Technology, The University of Hong Kong, Pokfulam road, Hong Kong, China. [2]Guangdong Provincial Key Laboratory of Quantum Metrology and Sensing & School of Physics and Astronomy, Sun Yat-sen University, Zhuhai Campus, Zhuhai, 519082, China. [3]State Key Laboratory of Optoelectronic Materials and Technologies, Sun Yat-sen University, Guangzhou Campus, Guangzhou, 510275, China. [4]Advanced Materials Laboratory, National Institute for Materials Science, 1-1 Namiki, Tsukuba, 305-0044, Japan.

Received: 6 September 2024 Revised: 12 December 2024
Accepted: 13 January 2025 Published online: 06 February 2025

References

1. H. Park, et al., Observation of fractionally quantized anomalous Hall effect. Nature **622**(7981), 74–79 (2023)
2. Y. Cao, et al., Unconventional superconductivity in magic-angle graphene superlattices. Nature **556**(7699), 43–50 (2018)
3. Y. Cao, et al., Correlated insulator behaviour at half-filling in magic-angle graphene superlattices. Nature **556**(7699), 80–84 (2018)
4. Z. Lian, et al., Valley-polarized excitonic Mott insulator in WS2/WSe2 moiré superlattice. Nat. Phys. **20**(1), 34–39 (2024)
5. E.C. Regan, et al., Mott and generalized Wigner crystal states in WSe2/WS2 moiré superlattices. Nature **579**(7799), 359–363 (2020)
6. Y. Tang, et al., Simulation of Hubbard model physics in WSe2/WS2 moiré superlattices. Nature **579**(7799), 353–358 (2020)
7. Y. Xu, et al., Correlated insulating states at fractional fillings of moiré superlattices. Nature **587**(7833), 214–218 (2020)
8. X. Huang, et al., Correlated insulating states at fractional fillings of the WS2/WSe2 moiré lattice. Nat. Phys. **17**(6), 715–719 (2021)
9. C. Jin, et al., Stripe phases in WSe2/WS2 moiré superlattices. Nat. Mater. **20**(7), 940–944 (2021)
10. S. Miao, et al., Strong interaction between interlayer excitons and correlated electrons in WSe2/WS2 moiré superlattice. Nat. Commun. **12**(1) (2021)
11. R. Xiong, et al., Correlated insulator of excitons in WSe2/WS2 moiré superlattices. Science **380**(6647), 860–864 (2023)
12. P. Rivera, et al., Observation of long-lived interlayer excitons in monolayer MoSe2–WSe2 heterostructures. Nat. Commun. **6**(1), 6242 (2015)
13. J. Kim, et al., Correlation-driven nonequilibrium exciton site transition in a WSe2/WS2 moiré supercell. Nat. Commun. **15**(1) (2024)
14. J. Kim, et al., Observation of ultralong valley lifetime in WSe2/MoS2 heterostructures. Sci. Adv. **3**(7), e1700518 (2017)
15. C. Jin, et al., Imaging of pure spin-valley diffusion current in WS2-WSe2 heterostructures. Science **360**(6391), 893–896 (2018)
16. L.J. McGilly, et al., Visualization of moiré superlattices. Nat. Nanotechnol. **15**(7), 580–584 (2020)
17. J. Sung, et al., Broken mirror symmetry in excitonic response of reconstructed domains in twisted MoSe2/MoSe2 bilayers. Nat. Nanotechnol. **15**(9), 750–754 (2020)
18. V.V. Enaldiev, et al., Stacking Domains and Dislocation Networks in Marginally Twisted Bilayers of Transition Metal Dichalcogenides. Phys. Rev. Lett. **124**(20) (2020)
19. A. Weston, et al., Atomic reconstruction in twisted bilayers of transition metal dichalcogenides. Nat. Nanotechnol. **15**(7), 592–597 (2020)
20. S. Shabani, et al., Deep moiré potentials in twisted transition metal dichalcogenide bilayers. Nat. Phys. **17**(6), 720–725 (2021)
21. S. Zhao, et al., Excitons in mesoscopically reconstructed moiré heterostructures. Nat. Nanotechnol. **18**(6), 572–579 (2023)
22. M.R. Rosenberger, et al., Twist angle-dependent atomic reconstruction and moiré patterns in transition metal dichalcogenide heterostructures. ACS Nano **14**(4), 4550–4558 (2020)
23. H. Li, et al., Imaging moiré flat bands in three-dimensional reconstructed WSe2/WS2 superlattices. Nat. Mater. **20**(7), 945–950 (2021)
24. D.A. Cosma, et al., Moiré pattern as a magnifying glass for strain and dislocations in van der Waals heterostructures. Faraday Discuss. (2014)
25. A. Falin, et al., Mechanical properties of atomically thin tungsten dichalcogenides: WS2, WSe2, and WTe2. ACS Nano **15**(2), 2600–2610 (2021)
26. H. Zhu, et al., Interfacial charge transfer circumventing momentum mismatch at two-dimensional van der Waals heterojunctions. Nano Lett. **17**(6), 3591–3598 (2017)
27. C. Jin, et al., Ultrafast dynamics in van der Waals heterostructures. Nat. Nanotechnol. **13**(11), 994–1003 (2018)
28. X. Hong, et al., Ultrafast charge transfer in atomically thin MoS2/WS2 heterostructures. Nat. Nanotechnol. **9**(9), 682–686 (2014)
29. F. Ceballos, et al., Ultrafast charge separation and indirect exciton formation in a MoS2–MoSe2 van der Waals heterostructure. ACS Nano **8**(12), 12717–12724 (2014)
30. J.E. Zimmermann, et al., Ultrafast charge-transfer dynamics in twisted MoS₂/WSe₂ heterostructures. ACS Nano **15**(9), 14725–14731 (2021)
31. H. Park, et al., Dipole ladders with large Hubbard interaction in a moiré exciton lattice. Nat. Phys. **19**(9), 1286–1292 (2023)
32. C. Jin, et al., Observation of moiré excitons in WSe2/WS2 heterostructure superlattices. Nature **567**(7746), 76–80 (2019)
33. F. Wu, T. Lovorn, A.H. Macdonald, Topological Exciton Bands in Moiré Heterojunctions. Phys. Rev. Lett. **118**(14) (2017)
34. S. Brem, et al., Tunable phases of moiré excitons in van der Waals heterostructures. Nano Lett. **20**(12), 8534–8540 (2020)
35. H. Yu, et al., Moiré excitons: from programmable quantum emitter arrays to spin-orbit–coupled artificial lattices. Sci. Adv. **3**(11), e1701696
36. M.H. Naik, et al., Intralayer charge-transfer moiré excitons in van der Waals superlattices. Nature **609**(7925), 52–57 (2022)
37. Z. Nie, et al., Ultrafast carrier thermalization and cooling dynamics in few-layer MoS2. ACS Nano **8**(10), 10931–10940 (2014)
38. T. Yan, et al., Probing the exciton k-space dynamics in monolayer tungsten diselenides. 2D Mater. **6**(2), 025035 (2019)
39. V.R. Policht, et al., Time-domain observation of interlayer exciton formation and thermalization in a MoSe2/WSe2 heterostructure. Nat. Commun. **14**(1) (2023)
40. Z.E. Eroglu, et al., Ultrafast dynamics of exciton formation and decay in two-dimensional tungsten disulfide (2D-WS(2)) monolayers. Phys. Chem. Chem. Phys. **22**(30), 17385–17393 (2020)
41. P.D. Cunningham, et al., Photoinduced bandgap renormalization and exciton binding energy reduction in WS2. ACS Nano **11**(12), 12601–12608 (2017)
42. E.A.A. Pogna, et al., Photo-induced bandgap renormalization governs the ultrafast response of single-layer MoS2. ACS Nano **10**(1), 1182–1188 (2016)
43. G. Aivazian, et al., Many-body effects in nonlinear optical responses of 2D layered semiconductors. 2D Mater. **4**(2), 025024 (2017)
44. K. Xiao, et al., Exciton-exciton interaction in monolayer MoSe2 from mutual screening of Coulomb binding. ACS Nano **18**(46), 31869–31876 (2024)
45. K. Xiao, et al., Exciton-exciton Interaction in Monolayer $MoSe_2$ from Mutual Screening of Coulomb Binding (2023). https://doi.org/10.48550/arXiv.2308.14362. arXiv:2308.14362
46. P. Rivera, et al., Valley-polarized exciton dynamics in a 2D semiconductor heterostructure. Science **351**(6274), 688–691 (2016)
47. X. Wang, et al., Intercell moiré exciton complexes in electron lattices. Nat. Mater. **22**(5), 599–604 (2023)
48. H. Chen, et al., Ultrafast formation of interlayer hot excitons in atomically thin MoS2/WS2 heterostructures. Nat. Commun. **7**(1), 12512 (2016)

Publisher's Note